Clim Dyn (2011) 37:1381–1398
DOI 10.1007/s00382-010-0915-y

Quantifying uncertainties in projections of extremes—a perturbed land surface parameter experiment

Erich M. Fischer · David M. Lawrence · Benjamin M. Sanderson

Received: 20 May 2010 / Accepted: 14 September 2010 / Published online: 16 October 2010

Abstract Uncertainties in the climate response to a doubling of atmospheric CO_2 concentrations are quantified in a perturbed land surface parameter experiment. The ensemble of 108 members is constructed by systematically perturbing five poorly constrained land surface parameters of global climate model individually and in all possible combinations. The land surface parameters induce small uncertainties at global scale, substantial uncertainties at regional and seasonal scale and very large uncertainties in the tails of the distribution, the climate extremes. Climate sensitivity varies across the ensemble mainly due to the perturbation of the snow albedo parameterization, which controls the snow albedo feedback strength. The uncertainty range in the global response is small relative to perturbed physics experiments focusing on atmospheric parameters. However, land surface parameters are revealed to control the response not only of the mean but also of the variability of temperature. Major uncertainties are identified in the response of climate extremes to a doubling of CO_2. During winter the response both of temperature mean and daily variability relates to fractional snow cover. Cold extremes over high latitudes warm disproportionately in ensemble members with strong snow albedo feedback and large snow cover reduction. Reduced snow cover leads to more winter warming and stronger variability decrease. As a result uncertainties in mean and variability response line up, with some members showing weak and others very strong warming of the cold tail of the distribution, depending on the snow albedo parametrization. The uncertainty across the ensemble regionally exceeds the CMIP3 multi-model range. Regarding summer hot extremes, the uncertainties are larger than for mean summer warming but smaller than in multi-model experiments. The summer precipitation response to a doubling of CO_2 is not robust over many regions. Land surface parameter perturbations and natural variability alter the sign of the response even over subtropical regions.

Keywords Climate extremes · Uncertainties · Heat waves · Land–atmosphere interactions · Snow albedo feedback · Parametrization

Electronic supplementary material The online version of this article (doi:10.1007/s00382-010-0915-y) contains supplementary material, which is available to authorized users.

E. M. Fischer (✉) · D. M. Lawrence · B. M. Sanderson
National Center for Atmospheric Research,
P.O. Box 3000, Boulder, CO 80302, USA
e-mail: efischer@ucar.edu

D. M. Lawrence
e-mail: dlawren@ucar.edu

B. M. Sanderson
e-mail: bsander@ucar.edu

E. M. Fischer
Institute for Atmospheric and Climate Science,
ETH Zurich, Zurich 8092, Switzerland

1 Introduction

Changes in the frequency and intensity of climate extremes have socio-economic impacts that reach far beyond the effects of mean warming. Numerous studies have explored changes in extreme temperature events during the observational period (e.g. Kunkel et al. 1999; Easterling et al. 2000; Meehl et al. 2000; Tebaldi et al. 2006). The most robust changes include a significant trend towards fewer cold nights and frost days and a tendency for more warm nights and heat waves (e.g. Frich et al. 2002; Alexander et al. 2006). Scenarios project an intensification of these

trends leading to more frequent, intense and longer lasting heat waves if atmospheric greenhouse gas concentrations continue to rise (e.g. Meehl and Tebaldi 2004; Schär et al. 2004; Beniston 2004; Weisheimer and Palmer 2005; Tebaldi et al. 2006; Kharin et al. 2007).

The magnitude of these projected changes in extremes, however, involves large uncertainties, particularly at regional scale. Uncertainties in climate projections arise from three distinct sources: (1) uncertainties in emissions of greenhouse gases and aerosols, and land use changes (scenario uncertainties), (2) the resulting atmospheric radiative forcing and the representation of the numerous feedbacks on the climate system in models (model uncertainties), and (3) natural variability (initial condition uncertainties). The latter two sources of uncertainty have mostly been addressed by considering the spread across an ensemble of opportunity, e.g. a relatively small ensemble of Global Climate Model (GCM) results (Tebaldi and Knutti 2007). However, such multi-model ensembles may substantially underestimate the actual uncertainty, since they are not designed to sample the full range of possible behaviours (Allen et al. 2000; Knutti et al. 2008; Hawkins and Sutton 2009). Moreover, it is difficult to determine whether differences identified in a multi-model ensemble arise from different initial conditions, structural uncertainties (such as grid resolution and the representation of processes) or uncertainties in the parameterization of subgrid scale processes (such as cloud formation).

Parameter uncertainties can be systematically quantified in perturbed physics ensembles (PPE), which are constructed by varying model parameters whose values cannot be accurately constrained by observations (e.g. Allen et al. 2000; Murphy et al. 2004; Piani et al. 2005; Stainforth et al. 2005). Using PPE it has been demonstrated that uncertainty range of climate sensitivity (the equilibrium response of global temperatures to a doubling of CO_2) induced by parameter choices in some GCMs is nearly as large or even larger than it is for a multi-model ensemble sampling across different GCMs (Murphy et al. 2004; Stainforth et al. 2005). PPE have further been used to quantify uncertainties in climate extremes, such as heat waves (Clark et al. 2006; Barnett et al. 2006), wet days (Barnett et al. 2006) and droughts (Burke and Brown 2008). While most of the available PPEs have been based on HadSM3, Sanderson (2010) demonstrates that a corresponding ensemble based on a different GCM (CCSM3.5) may yield a substantially smaller uncertainty range.

While most of the existing PPEs emphasize the role of atmospheric model parameterizations, we focus here on land surface model parameterizations. To our knowledge this is the first study systematically focusing on land surface parameter uncertainties in a global coupled model framework. Land surface parameter uncertainty analyses have been carried out in single column model (e.g. Liu et al. 2005) and offline experiments. The PPE evaluated in this study consists of 108 model versions (hereafter referred to as members), which are generated by systematically perturbing five land surface parameters in the land surface scheme of the Community Climate System Model (CCSM 3.5). Most of the land surface processes and their interactions with the atmosphere act on subgrid scales and need to be parameterized. The land surface parameters are generally poorly constrained by observations and represent an important source of uncertainty, which to our knowledge has not yet been systematically assessed in a coupled model framework.

Land surface parameterizations control the surface energy and water budgets and are crucial for a realistic representation of the present-day climate. Feedback mechanisms through snow albedo (e.g Qu and Hall 2006), soil moisture (Koster et al. 2002; Seneviratne et al. 2006a; Vidale et al. 2007) or vegetation change may amplify or offset future changes in mean temperature and its variability.

Here, we systematically quantify uncertainties induced by land surface parameters. We specifically focus on uncertainties in regional projections of temperature, precipitation and impact-relevant extremes. This controlled exercise further allows us to disentangle the relevance of individual land surface parameters. Particularly important parameters can be identified, thereby isolating which parameters need to be better constrained by observations to ultimately reduce uncertainties in projections.

The paper is organized as follows: First, the experimental setup, including the individual parameter perturbations, is detailed and an analysis of the primary impacts in single perturbation experiments is presented. Second, uncertainties in simulated temperature mean and variability are evaluated. Third, regional projections in temperature extremes are explored and finally, the precipitation response and related uncertainties are discussed.

2 CLMCUBE experiment

A 108-member perturbed parameter experiment (hereafter CLMCUBE) is performed with the NCAR Community Climate System Model (CCSM 3.5) (Gent et al. 2010) version with a non-dynamic mixed layer (slab) ocean. The finite volume model version used in this experiment has a horizontal resolution of 2° latitude × 2.5° longitude with 26 levels on hybrid vertical coordinates. The land surface model component is the Community Land Model (CLM), which is documented in detail in Oleson et al. (2004). The modifications in the latest version CLM 3.5 used here and its performance are described in Lawrence et al. (2007); Oleson et al. (2008); Stöckli et al. (2008). Subgrid-scale land surface heterogeneity is represented in CLM through

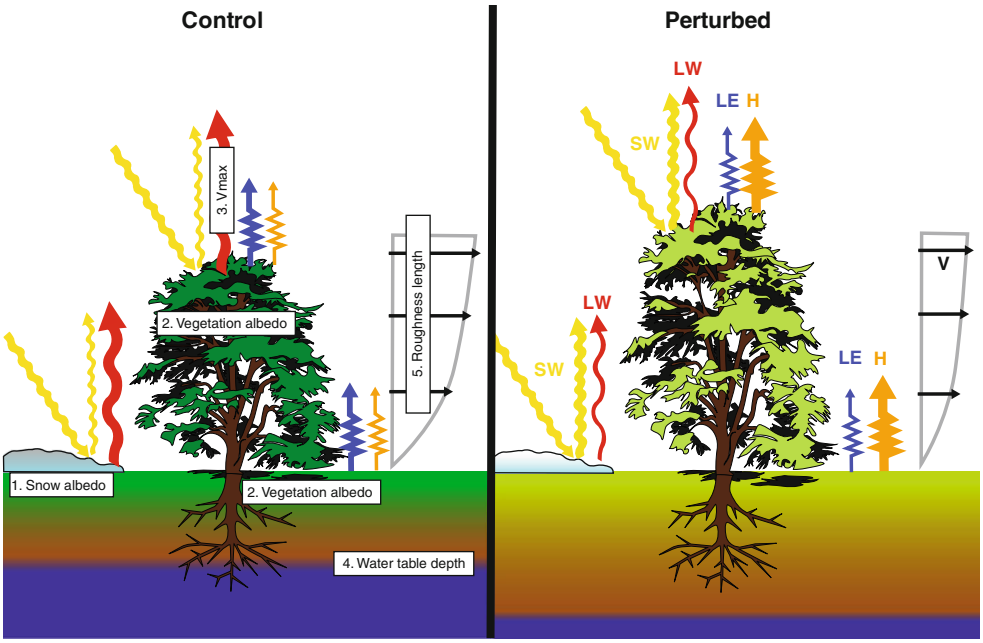

Fig. 1 Illustration of land surface model parameter perturbations and first order effects of shortwave (SW), longwave (LW), latent heat (LE) and sensible heat (H) fluxes (*colored arrows*) as described in Sect. 2

different fractional coverage of bare soil, lake, glacier, and vegetation. Vegetation cover is subdivided in 16 different plant functional types (PFTs) and the soil consists of 10 layers, which extend to a total depth of 3.4 m.

The basic experimental setup of CLMCUBE is similar to climateprediciton.net (Stainforth et al. 2005), the QUMP experiments (Murphy et al. 2004) and CAMCUBE (Sanderson 2010). Each CLMCUBE member simulation consists of three stages: a calibration, a 1 $\times$ CO_2 and 2 $\times$ CO_2 stage. In the 15-year calibration stage the sea surface temperatures are prescribed to diagnose heat convergence fields, which can be applied during the two later stages. Since the mixed layer ocean model does not explicitly represent ocean dynamics, the ocean heat transport has to be prescribed as heat convergence. The 1 $\times$ CO_2 simulations cover a 30-year period with constant atmospheric CO_2 concentrations of 355 ppm and the 2 $\times$ CO_2 cover 20 years, forced with atmospheric CO_2 concentrations of 710 ppm.

In each ensemble member, land surface parameters were perturbed to a high and low value relative to the standard values used in CLM3.5. Standard parameters that are at the low or high end of the parameter uncertainty range are only perturbed to one side. The perturbations have been applied to five poorly constrained land surface parameters (described below) individually and in all possible combinations to account for nonlinear interactions. In contrast to previous experiments such as CAMCUBE, QUMP and climateprediction.net, CLMCUBE focuses on uncertainties induced by land surface parameters.

The five land surface parameters were selected in close consultation with the CLM model development group. They include two optical parameters that affect the surface albedo (vegetation and snow reflectance), two parameters that exert significant control on the partitioning of surface turbulent fluxes (soil hydrology decay factor f and a photosynthetic parameter V_{max}), and one parameter that affects turbulent energy exchange (momentum roughness length). The parameter perturbations are based on uncertainty ranges found in the reference literature of the standard CLM parameters and in the case of snow albedo and water table on expert judgement.

The imposed perturbations to the five parameters and their primary anticipated climate effects are illustrated in Fig. 1 and discussed in detail in the following.

2.1 Snow albedo

Snow albedo in CLM 3.5 is calculated for the visible and near-infrared radiative spectrum. The calculation is a function of a prescribed fresh snow albedo and subsequent snow aging, which accounts for dirt and soot effects as well as for snow grain growth. The fresh snow albedo $\alpha_{sno,\wedge,0}$ is comparatively well constrained by observations and is set at 0.95 for visual and 0.65 for near-infrared radiation.

The actual snow albedo is calculated as

$$\alpha_{sno,\wedge} = [1 - C_{\wedge} F_{age}] \alpha_{sno,\wedge,0}, \quad (1)$$

where F_{age} is the snow age and $C_{\wedge}$ is a constant. In contrast to the fresh snow albedo, $C_{\wedge}$ is a highly uncertain empirical

Table 1 Summary of land surface model parameter perturbations detailed in Sect. 2

Parameter	Lower	Low	Standard	High	Higher
Snow albedo					
$C_\wedge$ (VIS) (empirical const., visual)		0.02	0.2	0.38	
$C_\wedge$ (NIR) (empirical const., near-infrared)		0.05	0.5	0.85	
Leaf albedo					
α_{vis}^{leaf} (leaf reflectance, visual)		$\alpha_{vis,i}-20\%$	α_i	$\alpha_{vis,i}+20\%$	
α_{nir}^{leaf} (leaf reflectance, near-infrared)		$\alpha_{nir,i}-20\%$	α_i	$\alpha_{nir,i}+20\%$	
Water table					
f [m^{-1}] (decay factor)			1.0	1.75	2.5
$q_{drai,max}$ [$kg\ m^{-2}\ s^{-1}$] (max. subsurface runoff)			8.5×10^{-4}	6.5×10^{-4}	4.5×10^{-4}
V_{max}					
SLA_i (specific leaf area index)			SLA_i	$SLA_i + \sigma$	
$CN_{L,\ i}$ (leaf carbon:nitrogen ration)			$CN_{L,\ i}$	$CN_{L,\ i} + \sigma$	
Momentum roughness length					
$R_{z0m,\ i}$ (ratio of momentum roughness length)			$R_{z0m,\ i}$	$2{*}R_{z0m,\ i}$	

Detailed values for each plant functional type (denoted with index *i*) are given in Tables S1–S5

quantity. Standard values used in CLM 3.5 and perturbed values are given in Table 1 and S1.

As a primary effect this perturbation alters the short- and longwave radiation absorbed by snow-covered surfaces. The members with only this parameter perturbed, simulate an albedo change over the Northern Hemisphere, which is largest in mid-winter (January and February). The net radiation change is largest in late winter and spring due to higher insolation. The effect of the two-sided perturbation on all sky albedo is non-symmetric. The surface net radiation change is almost four times larger for the high than for the low snow albedo perturbation. However, the resulting global mean land temperature changes are very similar (±0.12 K). Regional temperatures over seasonally snow-covered regions are unsurprisingly much more sensitive (±2–4 K).

2.2 Vegetation albedo

The reflectance of vegetation is a combined measure of leaf and stem reflectance and calculated for each PFT as

$$\alpha_\wedge = \alpha_\wedge^{leaf} w_{leaf} + \alpha_\wedge^{stem} w_{stem}, \quad (2)$$

where $w_{leaf} = L/(L + S)$ and $w_{stem} = S/(L + S)$ with L and S being the exposed leaf/stem area index. Even though surface albedo can be measured from satellites, the actual values for the different vegetation types include substantial uncertainties. To account for these uncertainties the leaf reflectance has been perturbed by ±20% to the values listed in Table 1 and S2.

This perturbation of leaf albedo directly alters the radiation absorbed by the vegetation covered land surface. The individual perturbations of vegetation albedo alter the global land surface net radiation by −2.0 W/m^2 (vegetation albedo +20%) and +2.4 W/m^2 (vegetation albedo −20%), respectively. This results in a global land temperature change of ±0.16 K, which is substantially larger at regional scale and during specific seasons, especially over the corresponding summer hemisphere (±1–2 K). The maximum sensitivity of net radiation and temperature is found over Central and Eastern North America, which are predominantly covered by crop and broadleaf deciduous temperate trees.

2.3 Maximum rate of carboxylation V_{max}

The rates of photosynthesis in CLM 3.5 are calculated at the leaf scale for sunlit and shaded canopy fractions. The leaf photosynthesis is dependent on the leaf-scale maximum carboxylation capacity of Rubisco (V_{max}, µmol $CO_2 m^{-2}\ s^{-1}$). V_{max} is formulated as a function of the leaf area based concentration of Rubisco and the enzyme activity as follows

$$V_{max} = \frac{1}{SLA \times CN_L} F_{LNR} \frac{1}{F_{NR}} a_R, \quad (3)$$

where SLA is the specific leaf area, CN_L the leaf carbon:nitrogen ratio gC gN^{-1}, F_{LNR} the fraction of leaf nitrogen in Rubisco (unitless), F_{NR} the mass ratio of nitrogen in the Rubisco molecule to total molecular mass (unitless) and a_R the specific activity of Rubisco (µmol CO_2 $gRubisco^{-1}s^{-1}$) (Thornton and Zimmermann 2007). Detailed observations of SLA and CN_L are presented in White et al. (2000) for different species. Measured values differ strongly across species of the same CLM PFT. The

standard parameter used in CLM 3.5 is typically the mean value for each PFT. Since photosynthesis in CLM 3.5 is generally considered to be high (Stöckli et al., 2008), we use a one-sided perturbation of SLA and CN_L of one standard deviation of the uncertainty given for each PFT in White et al. (2000) (see Table 1 and S3), which gives a smaller but still realistic V_{max}.

The perturbation of V_{max} directly affects photosynthesis and thereby leaf stomatal resistance. In the single perturbation simulation, modified V_{max} regionally decreases the ecosystem net photosynthesis by 50%. Note that here, due to the absence of an interactive carbon cycle model, this does not affect the atmospheric CO_2 concentrations. However, the higher stomatal resistance reduces plant transpiration globally by 3.7 W/m^2. This reduction is partly offset (40–50%) by enhanced bare soil evaporation. As a result, the global latent (sensible) heat flux over land is reduced (enhanced) by about 2W/m^2. Regionally the change in partitioning of turbulent fluxes is substantially larger, peaking at 15–20W/m^2 over eastern North America during summer (see map in Fig. S1a).

2.4 Water table depth and subsurface runoff

The surface and subsurface runoff are calculated with a simple TOPMODEL-based runoff scheme (SIMTOP) (Niu et al. 2005). The determination of the water table depth z_∇ is based on a simple groundwater model by Niu et al. (2007). The groundwater solution is dependent on whether the water table is within or below the soil column (3.4 m). The water table depth affects subsurface and surface runoff generation and thereby soil hydrology, which in turn controls the surface energy and water budget.

The subsurface runoff or drainage q_{drai} in CLM 3.5 is defined as follows:

$$q_{drai} = (1 - f_{imp}) q_{drai,max} \exp(-f z_\nabla), \quad (4)$$

where f_{imp} is the fraction of impermeable area determined from the ice content of the soil layers, $q_{drai,max}$(kg m^{-2} s^{-1}) is the maximum subsurface runoff when the grid-averaged water table depth equals zero (i.e. is at the surface) and f is a decay factor, which was determined through sensitivity analysis and comparison against observed runoff data.

Both the decay factor f and $q_{drai,max}$ are perturbed in combination. Generally an increase in f decreases the water table depth, which results in wetter soils and lower subsurface runoff, whereas larger $q_{drai,max}$ results in drier soils. Since the water table depth has been found to be generally shallow with standard parameters of CLM 3.5 (Oleson et al. 2008), one-sided perturbations are applied. The standard values and the perturbations are given in Table S4.

The primary effect of the one-sided perturbation of the soil hydrological parameters f and $q_{drai,max}$ is an increase of the water table depth (average +0.6 for moderate, and +2.4 m for maximum perturbation, respectively) and lead to higher subsurface and lower surface runoff. On average the drier soils lead to slightly higher surface albedo. Latent heat flux over land is reduced by 2.8 W/m^2 in the member with maximum perturbations, mainly due to reduced bare soil evaporation (see spatial pattern of latent heat flux anomaly in Fig. S1a). In response, global land precipitation is slightly reduced and precipitation minus evaporation is substantially lower. The enhanced sensible heat flux results in a warming of mean land temperatures by 0.28 K, the strongest temperature signal induced by a single parameter perturbation. The spatial temperature anomaly pattern is more uniform than in the case of the other perturbations.

2.5 Roughness length

The roughness lengths for momentum (z_{0m}), heat (z_{0h}) and water vapor flux (z_{0w}) are equal and calculated as follows

$$z_{0m} = z_{0h} = z_{0w} = z_{top} R_{z0m}, \quad (5)$$

where z_{top} is the canopy top height for the plant functional type and R_{z0m} the ratio of momentum roughness length. While the canopy top height is relatively well constrained by observations, the ratio of momentum roughness length varies substantially across GCMs. For some PFTs the actual roughness lengths used in CLM 3.5 is less than half of the values used in the ECMWF land surface scheme TESSEL (ECMWF 2007). To account for this uncertainty, we double the standard ratio R_{z0m} for each PFT (see Table S5).

The perturbation of roughness length primarily reduces the near surface wind speed but has a negligible effect on global land temperatures. Global land precipitation is slightly reduced by about 1%.

3 Extreme indices

The uncertainties in the response of climate extremes to a doubling of CO_2 are explored based on widely used indices. Most of the indices used here are introduced and defined in Frich et al. (2002) and also used in Tebaldi et al. (2006); IPCC (2007). The extreme indices are briefly defined in the following:

- *Tropical nights (TR)*: Total number of tropical nights (i.e. days with absolute minimum temperatures >20°C).
- *Heat wave duration index (HWDI)*: maximum period of at least 6 consecutive days (within summer months May–September for Northern Hemisphere, and November–March for Southern Hemisphere, respectively) with maximum temperatures more than 5°C

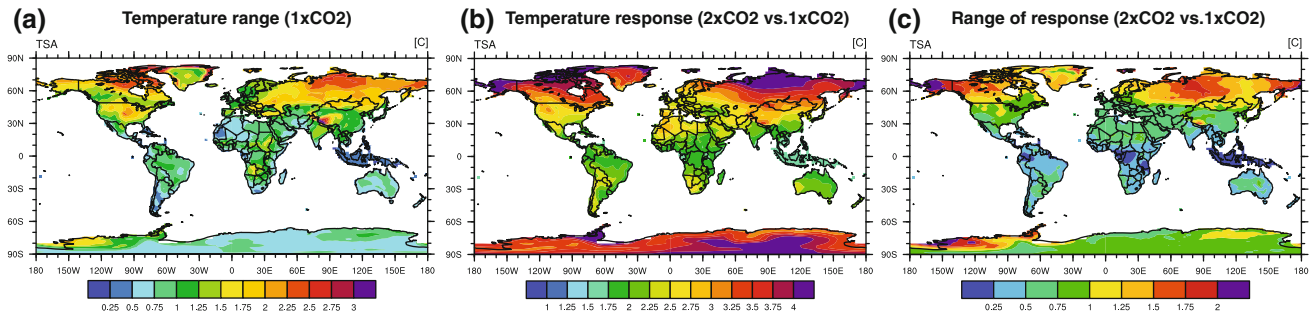

Fig. 2 CLMCUBE ensemble range of present-day annual mean temperatures (*left*, displayed as the local difference between 5th and 95th percentile member). Ensemble mean annual temperature response to doubling of CO_2 (*central*) and corresponding ensemble range (*right*, 5th-95th percentile)

warmer than reference value. The reference value is a centered mean of daily maximum temperatures over a 5-day time window derived from the corresponding present-day (1 × CO_2) simulation.

- *Heat index days warmer than 40.6°C/105°F (HI105F)*: the average number of days with maximum humidity-corrected heat index (apparent temperature) exceeding 40.6°C (105F). The heat index (Steadman 1984), represents heat stress on the human body by accounting for the effects of additional environmental factors beyond temperature. Here we use an approximated version of the heat index defined in detail in Fischer and Schär (2010) that accounts for ambient humidity under shaded conditions and that is commonly used by NOAA in North America (see http://www.crh.noaa.gov/pub/heat.php).
- *Frost days (FD)*: Total number of frost days (i.e. days with absolute minimum temperatures <0°C) per year.
- *Growing season length (GSL)*: number of days between the first occurrence of at least 6 days with mean temperatures >5°C and the first occurrence (after July 1) of at least 6 days with mean temperatures <5°C. GSL is not defined and thus not shown for regions outside the Northern extratropics.

All of the above indices are calculated on annual or seasonal basis and then averaged over the entire 1 × CO_2 and 2 × CO_2 simulation period.

4 Land surface parameter effect on mean temperature

4.1 Sensitivity of present-day temperatures

Here, we evaluate the sensitivity of land temperatures in present-day climate (1 × CO_2) to parameter perturbations. The temperature range across CLMCUBE is depicted as the local annual mean difference between the 95th and 5th percentiles of all 108 ensemble members (Fig. 2a). The sensitivity of present-day temperatures (annual, DJF and JJA mean) to the perturbation is smallest in the tropics and largest in the northern high latitudes and the Tibetan Plateau. JJA temperatures are also highly sensitive over northern mid-latitudes at about 40–50°N (not shown).

The sensitivity to each parameter is assessed by averaging all members with high/low value for each parameter (e.g. 36 low vs. 36 high vegetation albedo members). The composite difference qualitatively agrees with the difference patterns of the individual parameter perturbations runs. However, averaging over all members reduces the internal variability and leads to a smoother difference field. Composite temperature difference for each of the five perturbed parameters are shown in Fig. S2. Snow albedo is the dominant parameter explaining the annual mean temperature differences in northern high latitudes (1–1.5 K north of 60°N), and vegetation albedo in mid-latitudes (0.6–1 K at 30–60°N). V_{max} and water table depth have a moderate effect on annual temperatures ($\sim$0.3–0.5 K) over most of the continents.

The sensitivity of summer temperatures to the different parameters is rather complex and varies across regions and seasons. We calculate the relative variance explained by each of the five parameters (predictor) for regional summer temperature (predictand) based on a multiple linear regression (see Table 2). The linearity assumption of this approach is found to be well justified for the present-day temperatures (in contrast to the response to 2 × CO_2, see below).

Vegetation albedo explains the highest variance in summer temperatures throughout northern mid-latitudes through its control on net radiation. Summer temperatures are also sensitive to V_{max} over the Amazon Basin, and to water table depth, particularly in dry regions (e.g. Central Asia, the Mediterranean Basin, Western Africa and Australia). Both these parameters control evapotranspiration, modify the Bowen ratio and thereby affect the local summer temperatures.

Table 2 Role of different land surface parameters in explaining ensemble range of summer (JJA for Northern Hemisphere and DJF for Australia) temperatures derived from multiple linear regression

	Total expl. var.	Veg. albedo	Snow albedo	Water table	V_{max}	Roughn. length
Summer temp.						
AUS	63.8	12.6	0.0	32.4	19.9	0.6
AMZ	92.0	23.6	0.0	15.1	46.6	7.0
WNA	97.1	53.6	4.2	17.0	20.5	1.9
CNA	97.0	60.1	1.3	13.5	21.9	0.3
ENA	97.0	50.0	2.1	7.7	37.3	0.0
MED	97.2	59.3	1.8	23.3	12.6	0.3
NEU	92.1	44.2	3.6	14.6	29.7	0.4
WAF	80.0	21.8	0.0	33.5	22.6	2.9
SAS	67.3	16.8	0.1	9.4	21.5	21.1
CAS	97.5	56.1	2.1	27.2	11.9	0.3
NAS	97.6	45.6	13.1	12.5	26.4	0.1

The total adjusted variance [%] is given in the first column and the partial variance [%] explained by each parameter in the following columns. Values are regionally averaged over Australia (AUS), Amazon Basin (AMZ), Western North America (WNA), Central North America (CNA), Eastern North America (ENA), Mediterranean Basin (MED), Northern Europe (NEU), Western Africa (WAF), South Asia (SAS), Central Asia (CAS), North Asia (NAS). The exact coordinates defining the regions are given in (IPCC 2007)

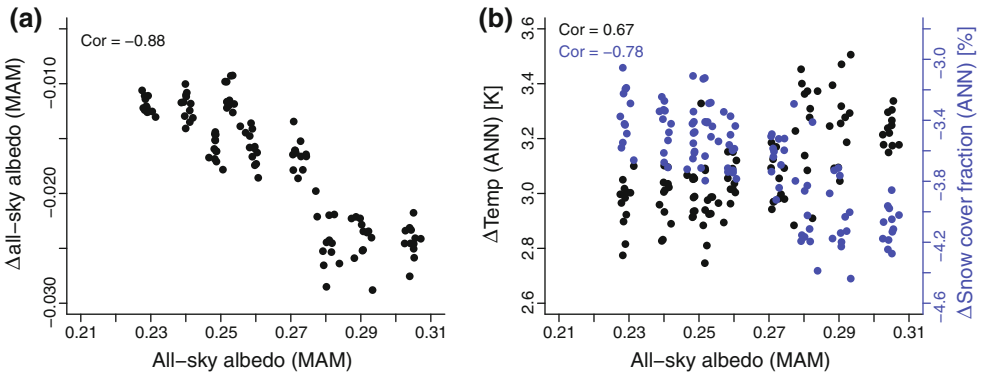

Fig. 3 (*left*) Correlation between present-day spring (MAM) all-sky albedo and corresponding response to a doubling of CO_2 in northern extratropics (30–90°N) across all CLMCUBE members. (*right*) Correlation between present-day spring (MAM) all-sky albedo and annual temperature response (*black*) and fractional snow cover reduction (*blue*) in northern extratropics

4.2 Uncertainty in response to a doubling of CO_2

The ensemble mean global land temperature response ΔT_{ANN} to a doubling of atmospheric CO_2 concentrations from 355 ppm to 710 ppm is 2.65 K. The full range of land temperature response across the land surface parameter perturbation experiments is 2.47 to 2.87 K. The uncertainty range of climate sensitivity (including ocean areas) across CLMCUBE is 2.04–2.33 K. This range is substantially smaller than in CAMCUBE (equilibrium climate sensitivity 2.2–3.2 K), the corresponding PPE with the same model but for perturbations across four atmospheric model parameters (Sanderson 2010). This confirms that the uncertainty in climate sensitivity induced by atmospheric parameters (affecting water vapour, lapse rate and cloud feedbacks) dominate over land surface parameter uncertainties.

We find that ΔT_{ANN} cannot be estimated by a linear combination of the impacts of the individual land surface parameter perturbations (e.g. same multiple linear regression as conducted above yields low explained variances). Since the multiple linear regression fails to explain the variance across the ensemble, we instead use a nonparametric recursive partitioning and regression method (Breiman et al. 1984) to identify the most important land surface parameter for ΔT_{ANN}. Snow albedo is found to explain the largest partial variance (43%) in ΔT_{ANN} across CLMCUBE.

Members with a higher present-day snow albedo (and higher snow cover fraction) simulate a stronger reduction in spring albedo and annual snow cover fraction (Fig. 3), which leads to a larger ΔT_{ANN} over northern extratropics (30°–90°N). We find a significant correlation ($r = 0.67$) between present-day all-sky albedo in the extratropics

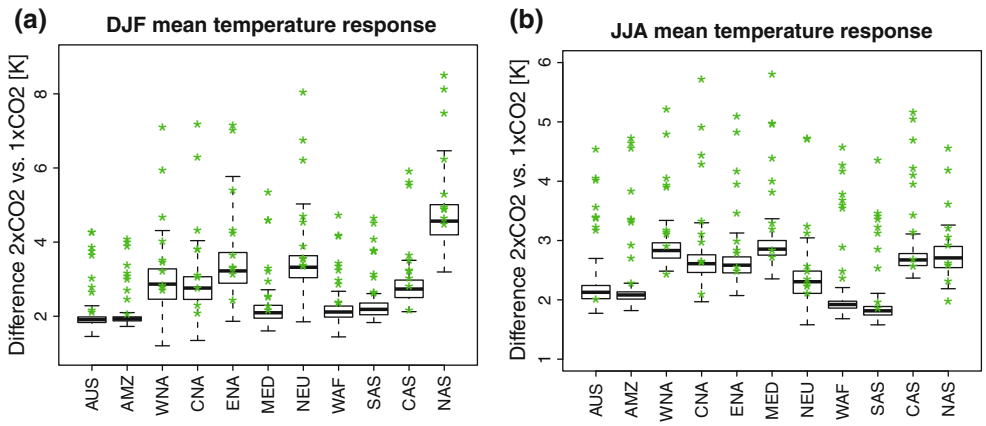

Fig. 4 Response in mean (**a**) DJF and (**b**) JJA temperatures in response to a doubling of CO_2 for regions defined in Table 2. The *boxes* indicate the 25th and 75th percentile of the ensemble range and the whiskers the most extreme members. *Green stars* show the corresponding response in ten CMIP3 models providing output for this equilibrium sensitivity slab ocean experiment

(30°–90°N in MAM) and ΔT_{ANN} across the ensemble. This is consistent with Levis et al. (2007) who suggested that models with a high (low) snow albedo bias have a strong (weak) snow albedo feedback and also tend to have a higher (lower) equilibrium climate sensitivity. Qu and Hall (2007) suggested that the snow albedo feedback in models with high present-day snow albedo is stronger as a result of the higher contrast between snow-covered and snow-free surfaces.

The uncertainty range of ΔT_{ANN} is largest (>2 K) over the northernmost latitudes (where the ensemble mean response ΔT_{ANN} is largest) and smallest over the tropics (Fig. 2b, c). Magnitude of response and uncertainty are not necessarily correlated, e.g. over Antarctica ΔT_{ANN} is large and the corresponding uncertainty identified here, comparatively small. The response in members with low present-day snow albedo is on average 0.5–1 K weaker than in members with high albedo (Fig. S3, upper left). Interestingly CLMCUBE also suggests comparatively weak high latitude warming in members with low vegetation albedo and deep water table (Fig. S3 upper middle and right panel).

The uncertainty range in winter warming (ΔT_{DJF}) is particularly high over Northern Europe (+1.9–5.0 K), Northern Asia (+3.2–6.5 K) and Alaska (+2.3–6.9 K) (Fig. 4a). This implies that simple land surface parameter perturbations can more than double ΔT_{DJF}, at least regionally. When compared to equilibrium climate sensitivity experiments performed with 10 CMIP3 models (Meehl et al. 2007), the uncertainty range in CLMCUBE regionally corresponds to about 50–80% of the multi-model ensemble range. Note that some portion of the uncertainty in the CLMCUBE arises from internal model variability, which due to the relatively short simulation length inflates the uncertainty range (Fig. S4b).

The uncertainty range of the JJA response (ΔT_{JJA}) is typically smaller (2.0–3.3 K over Central North America and 2.2–3.3 K over Northern Asia), which is only about 20–40% of the CMIP3 uncertainty range (Fig. 4b).

5 Land surface effect on temperature variability

Land surface parameters not only affect the mean state but also the variability of several climate variables at interannual to intraseasonal time scales (e.g. Seneviratne et al. 2006b; Fischer and Schär 2009). Such variability changes may affect the intensity of climate extremes beyond a simple shift in the mean climate (e.g. Katz and Brown 1992; Schär et al. 2004). Here we define temperature variability as the standard deviation of daily JJA and DJF temperatures over the entire simulation length.

Observed temperature variability (based on HadGHCND, Caesar et al. 2006) is generally small over the tropics and large over the high-latitudes (both in winter and summer) and over the northern mid-latitudes around 40–50° (summer only). CCSM 3.5 captures the observed latitudinal dependence of temperature variability reasonably well (not shown). The model somewhat overestimates the local variability maxima north of 60°N in DJF and over the northern subtropical regions in JJA.

Temperature variability is highly sensitive to parameter perturbations in CLMCUBE. In JJA the variability spread across CLMCUBE is largest over northernmost latitudes, the central United States as well as central and southern Europe (Fig. 5b). In the following we explore the dominant parameters and underlying mechanisms for selected regions of high variability.

Over mid-latitudes, vegetation albedo and water table depth are the dominant parameters in explaining JJA variability across CLMCUBE. Latent heat, which in this experiment is largely controlled by the water table depth,

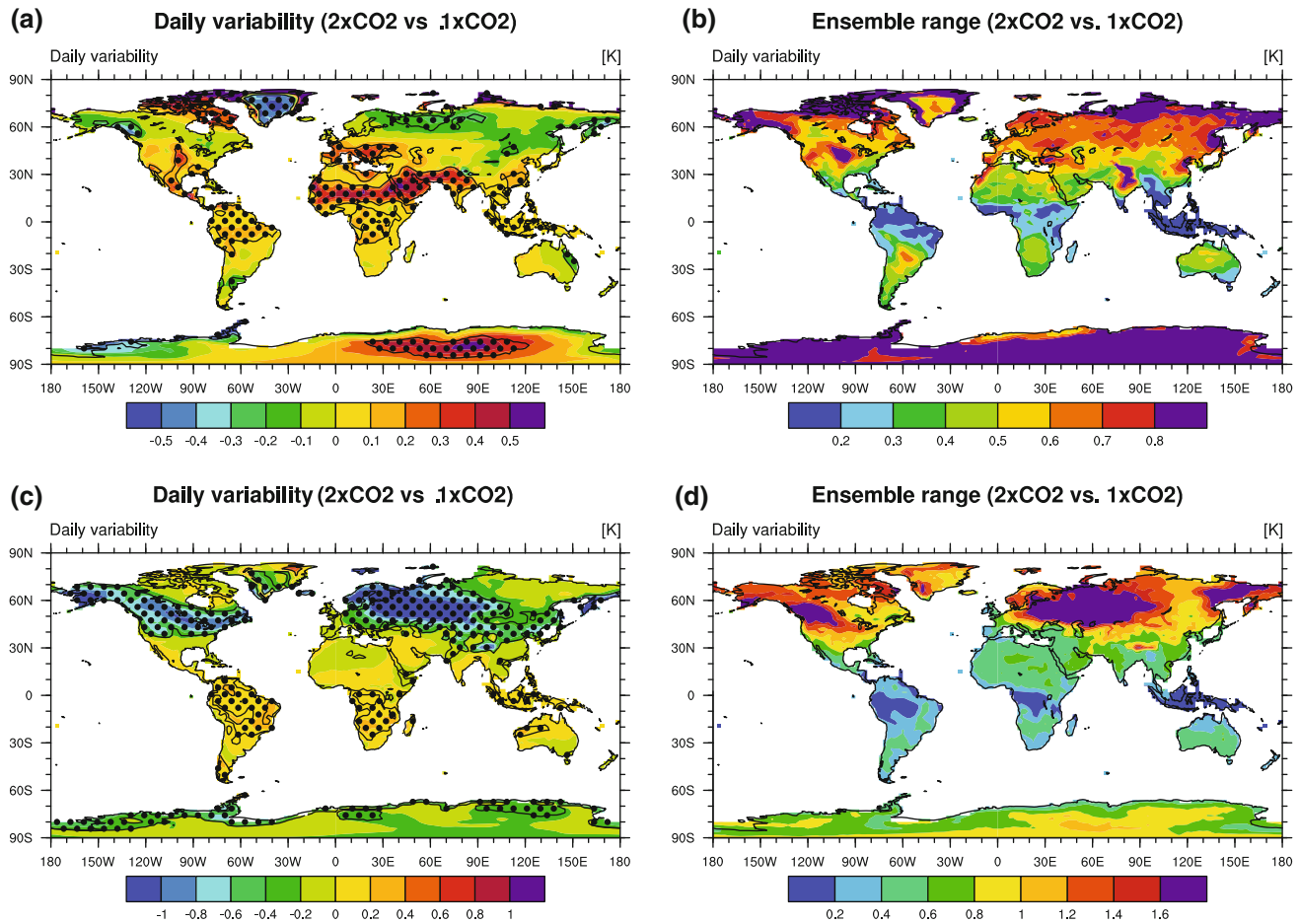

Fig. 5 Daily temperature variability change in JJA (*upper panels*) and DJF (*lower panels*) in response to a doubling of CO_2. Ensemble mean response (*left panels*) is shown along with respective ensemble range (5th–95th ensemble percentile, *right panels*). Grid points where the response is significant (*F*-test) at 95% confidence level in the majority of members are stippled

acts as a damping factor of daily temperature variability (Fischer and Schär 2009).

Gregory and Mitchell (1995) suggested that daily temperature variability is determined by the ratio of latent heat flux to the sum of the outgoing turbulent and longwave fluxes λ, which is defined as

$$\lambda = \frac{LE}{LE + H + LW} = \frac{LE}{SW + GH},$$

where *LE* is latent heat flux, *H* is sensible heat flux, *LW* is longwave surface net radiation, *SW* is shortwave surface net radiation, and *GH* is ground heat flux. In CLMCUBE we find a significant anticorrelation between λ and JJA variability over the Mediterranean and Central North America (Fig. 6a). Reduced *LE* (e.g. due to dry soils) tends to enhance daily summer temperature variability and increased *LE* tends to dampen it.

Diurnal temperature range (DTR) and daily variability share the same underlying mechanisms, which is substantiated by their strong correlation across CLMCUBE members (not shown). Relative humidity is highly anticorrelated with JJA variability and DTR over dry regions (Fig. 6b). Members with low relative humidity and high JJA mean temperatures simulate high daily variability (see also Fischer and Schär 2009). We suggest that variability and DTR are mainly linked to relative humidity through their dependence on cloudiness (see also Dai et al. 1999).

In response to $2 \times CO_2$, JJA variability tends to increase mostly over dry regions including Central North America and Mediterranean (Fig. 5a). Over the Mediterranean region more than 90% of the CLMCUBE members simulate enhanced variability. Temporal decomposition of the variability response reveals that the annual cycle is strongly enhanced due to a larger temperature contrast between early summer and the warmest period in late July and early August (see also Fischer and Schär 2009). Furthermore, the soil drying substantially increases day-to-day temperature variations through the mechanisms discussed above. The variability increase over the Sahel and Arabian Peninsula should not be overinterpreted as it occurs over an

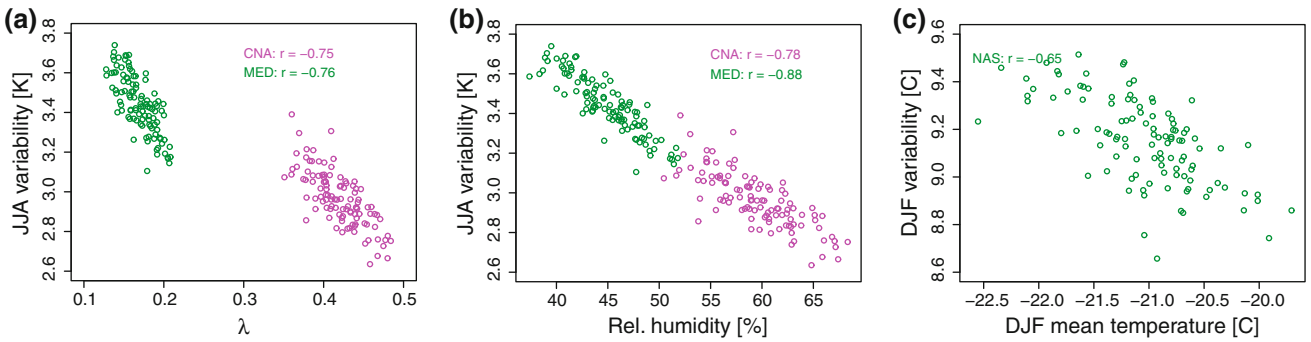

Fig. 6 **a** Correlation between present-day JJA daily temperature variability and λ in Central North America (CNA) and the Mediterranean Basin (MED). λ is defined as the ratio of latent heat to the sum of longwave, sensible and latent heat (see Sect. 5 for details). **b** Same as (**a**) but correlation between daily variability and relative humidity. **c** Correlation between present-day DJF daily temperature variability and mean temperature in North Asia. As in many other mid- to high-latitudinal regions, DJF mean and variability are highly correlated through snow cover

area of small present-day variability with a substantial wet bias in precipitation.

During DJF the ensemble range of present-day variability is largest at the edges of the area commonly covered by snow during winter at around 45–60°N. Winter temperature variability over these latitudes is significantly correlated with snow albedo and fractional snow cover. Cold, snow-covered regions characteristically have very low latent heat flux and atmospheric humidity, which otherwise tend to damp variability. Thus, DJF variability in regions such as Northern Asia is generally large in members with high albedo and low mean temperatures (Fig. 6c and S7).

In response to a doubling of CO_2 DJF variability is strongly reduced around 60°N (Fig. 5c), associated with the strongest reduction in fractional snow cover. This is consistent with changes at interannual scales (Gregory and Mitchell 1995; Räisänen, 2002). Variance decomposition reveals that DJF variability mostly changes at intraseasonal rather than longer time scales. CLMCUBE reveals large uncertainties in the response (Fig. 5d). Most members show a strong variability decrease and a few members no change or slightly enhanced variability. Members with strong warming and snow melt, tend to simulate a stronger variability reduction, which is consistent with the driving processes identified above.

6 Uncertainties in temperature extremes

Per definition the extremes have an infrequent and irregular nature and as a consequence long simulations are required to quantify their changes. In order to increase the robustness of our estimate, we here use moderate criteria. Note that because of their still relatively coarse resolution, GCMs may underestimate the intensity of extreme weather events, particularly for precipitation-related events (Räisänen and Joelsson 2001; Tebaldi et al. 2006). Here we first explore the intensity of hot and cold extremes, and second, changes in widely-used extreme indices.

6.1 Intensity of cold and hot extremes

Cold extremes are defined as 5th percentile of daily winter temperatures ($T5P_{DJF}$) and hot extremes as 95th percentile of summer temperatures ($T95P_{JJA}$). These represent two extremely cold/hot thresholds, which on average occur on 4–5 days per winter and summer, respectively.

All CLMCUBE members simulate strong temperature increases, $\Delta T95P_{JJA}$ and $\Delta T5P_{DJF}$, in response to a doubling of CO_2 (Fig. 7). Due to the reduced DJF variability over high latitudes, $\Delta T5P_{DJF}$ exceeds the mean winter warming regionally by up to a factor of 2. In Northern Europe and Northern Asia the $\Delta T5P_{DJF}$ is on average 60 and 20% larger, respectively, than the DJF mean warming. Interestingly, we find that mean warming and variability reduction are correlated across CLMCUBE, even though they are statistically independent. Lower snow cover fraction in response to a doubling CO_2 tends to reduce variability and amplify $\Delta T5P_{DJF}$. Thus, members showing a large mean warming tend to simulate a stronger variability reduction over mid- to high-latitudes. As a result, mean and variability uncertainties tend to line up, giving rise to very large uncertainties in $\Delta T5P_{DJF}$. Fig. 8 illustrates that in northern extratropics (30–90°N), and in particular in Northern Europe, members with a high ΔT_{DJF}, tend to simulate a strongly amplified $\Delta T5P_{DJF}$. In Northern Europe $\Delta T5P_{DJF}$ ranges between 1.9–8.8 K and in North Asia between 3.0–8.3 K (Fig. 7a). Thereby the CLMCUBE uncertainty range exceeds the spread of the six CMIP3 models (green stars), which provide daily output for this equilibrium sensitivity experiment.

Regarding summer hot extremes, $\Delta T95P_{JJA}$ is typically 15–20% larger than the mean summer warming over subtropical regions due to the enhanced JJA variability. This

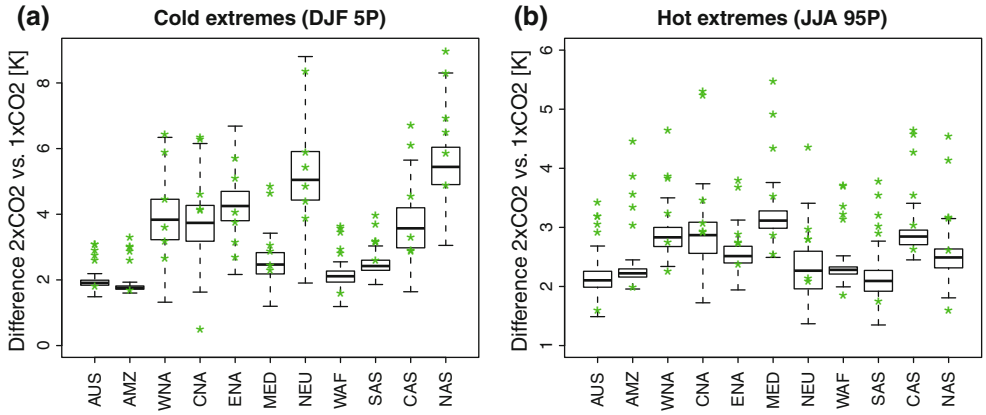

Fig. 7 Regional change in intensity of cold extremes (DJF 5th percentile) and hot extremes (JJA 95th percentile) in response to a doubling of CO_2 for regions defined in Table 2. The *boxes* indicate the 25th and 75th percentile of the ensemble range and the whiskers the most extreme members. *Green stars* show the corresponding response in six CMIP3 models providing daily output for this equilibrium sensitivity slab ocean experiment

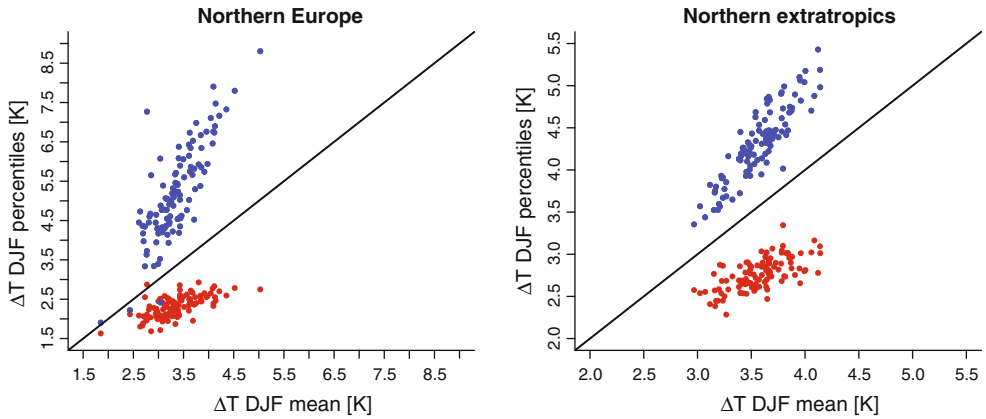

Fig. 8 Scatterplot of DJF mean temperature response versus DJF 5th (*blue*) and 95th percentile (*red*). Each point marks one member of the CLMCUBE ensemble. Temperatures are averaged over land grid points in (left) Northern Europe (see definition in Table 2) (right) northern extratropics (30–90°N)

difference in warming between highest percentile and mean summer temperature is consistent though less pronounced than in earlier PPE based on HadSM3 (Clark et al. 2006). Again, we find that the uncertainty range is larger for $\Delta T95P_{JJA}$ than ΔT_{JJA}. While in present-day runs, members with high mean temperatures tend to simulate high JJA variability, we do not find a significant correlation in their response. Over Central North America uncertainty range of $\Delta T95P_{JJA}$ is largest (1.6–3.6 K) (Fig. 7b), which is still substantially smaller than the spread in the CMIP3 models (green stars).

In summary uncertainties both in cold and hot extremes are substantially larger than the uncertainty in the mean. In winter the CLMCUBE range regionally exceeds the CMIP3 suite of models, whereas in summer it is substantially smaller.

The extreme temperature range (ETR) expresses the difference between hot and cold extremes discussed above. Thus, ETR is basically an extremes measure of the annual cycle and is highly correlated to the amplitude of the annual cycle defined as the difference between mean JJA and DJF temperatures. The CLMCUBE members simulate a statistically significant decrease in ETR over high-latitudes and a weak increase over subtropical regions. The ensemble mean ETR response pattern is in good agreement with the transient response of CCSM3.0 and CMIP3 multi-model mean at the end of the twenty-first century (Tebaldi et al. 2006). Due to the high uncertainties in both cold and hot extremes, ETR is highly sensitive to the CLM parameter perturbations, showing uncertainties even in the sign of the response over numerous regions (Fig. 9b).

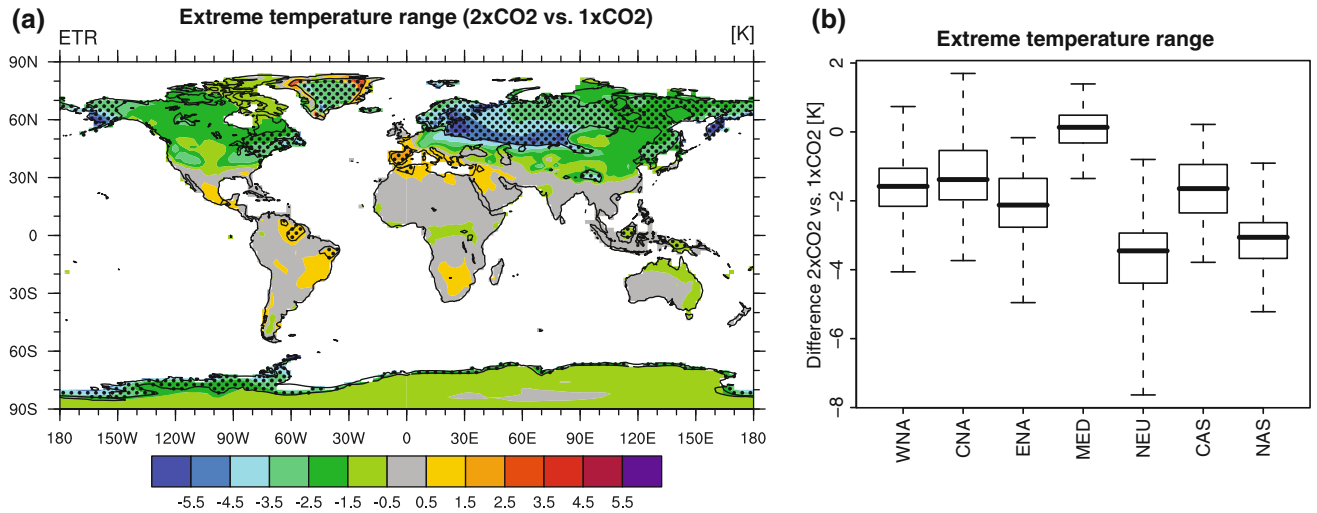

Fig. 9 Ensemble mean response in extreme temperature range to a doubling of CO_2 (*left*) and regional uncertainties (*right*) for regions defined in Table 2. Grid points where the response is significant at 95% confidence level in the majority of members are stippled

6.2 Heat waves and health indicators

In this section we discuss the response of three indices (see Sect. 3), which reflect different aspects of heat impacts on human discomfort and mortality: (1) high night-time temperatures (2) extended duration of a heat wave, and (3) relative humidity. Statistical studies (Hémon et al. 2003; Grize et al. 2005) suggest that the mortality increases due to very warm nights in which the human body cannot recover from excessive day time heat. The critical minimum temperature threshold differs across regions due to different adaptation levels. We here use a threshold of Tmin >20°C for tropical nights (TR), which is a well-established indicator for human discomfort during heat wave episodes.

The TR response to a doubling of CO_2 is largest over the tropical regions due to the high baseline values in present-day climate. Over northern mid-latitudes as well as in Australia all members simulate a severe increase of about 20–40 TR per year (Fig. 10a). Night-time temperatures are comparatively insensitive to land surface perturbations and thus the uncertainties identified through CLMCUBE are rather small (Fig. 10b).

Impacts on human health relate to a heat episode of an extended duration (several days) rather than a single extreme day. The heat wave duration index (HWDI) expresses the change in the longest heat wave per season. Severely enhanced HWDI are found over western and central North America, around the Mediterranean, in western Australia, South Africa and parts of South America (Fig. 10c). The increased duration is a very robust signal, however the exact magnitude of the response differs typically by a factor of 2–3 across the ensemble (Fig. 10d).

Finally, we consider the role of humidity, a well-established health factor during heat waves. Changes in relative humidity may in principle either amplify or offset the health effects of temperature extremes. The daily maximum heat index (apparent, human-perceived temperature) (Steadman 1984) accounts for the combined effect of temperature and humidity stress under shaded conditions.

Severe increases in dangerous heat index conditions (heat index >105F) are found over subtropical regions in both hemispheres. Large parts of Australia, the United States, North Africa and South Asia experience more dangerous health conditions in response to a doubling of CO_2 (increase by 10–40 days). Note that in the present-day climate simulations such conditions occur only on five days per year over most of these regions. While relative humidity is constant or slightly reduced in some of the above regions, the impact of the warming is not compensated for. Since the same mean warming leads to a stronger heat index increase over areas, which are humid and warm in present-day climate (Fischer and Schär 2010), the coastal areas experience the strongest heat index changes. The heat index response involves substantial uncertainties, however the uncertainties may still be regarded as surprisingly low. The reason here is that members with higher temperatures tend to simulate lower relative humidity and vice versa (not shown). As a result their uncertainties tend to counter each other and the uncertainty in heat index response is smaller than if the two variables were independent.

The above indices describe changes in the exceedance frequency of fixed or relative (percentile-based) thresholds. In contrast to changes in intensity, frequency changes are comparatively insensitive to variability and mainly dependent on mean changes (Barnett et al. 2006; Fischer and Schär 2010).

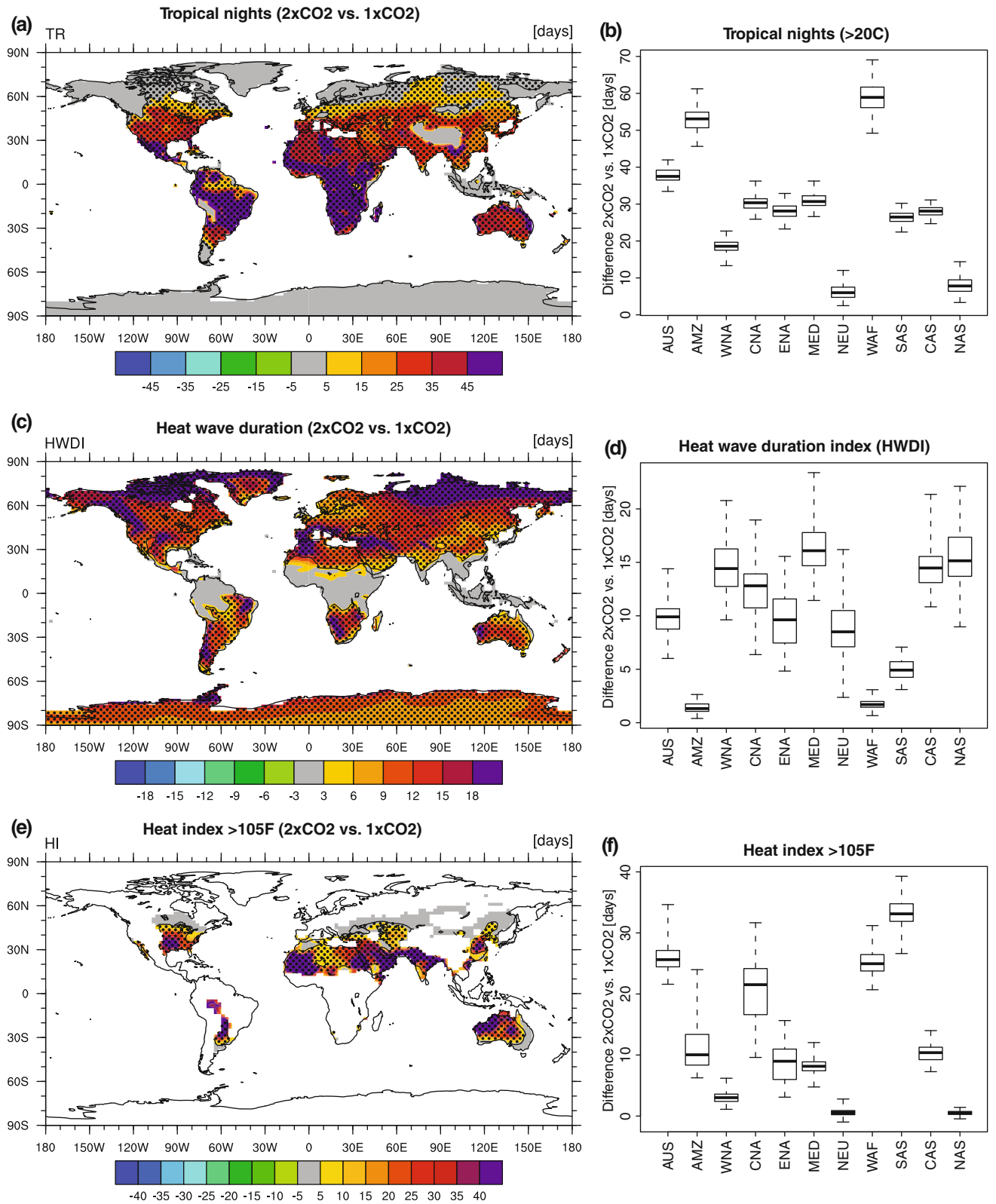

Fig. 10 Ensemble mean change in number of tropical nights (TR), heat wave duration index (HWDI) and number of days when the heat index exceeds 40.6°C /105°F in response to a doubling of CO_2 (*left*) and regional uncertainties (*right*) for regions defined in Table 2. Grid points where the response is significant at 95% confidence level in the majority of members are stippled

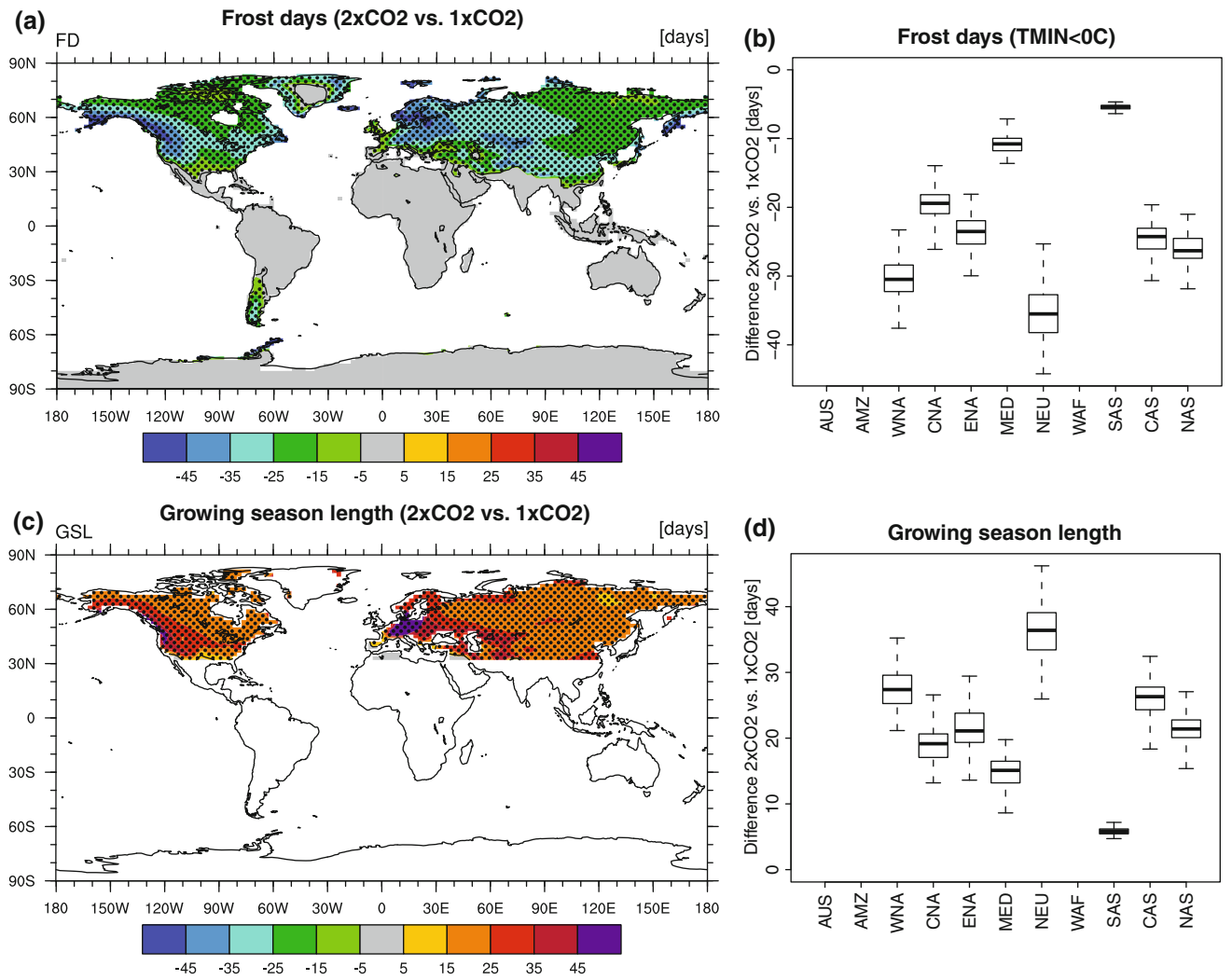

Fig. 11 Ensemble mean change in number of frost days (FD) and growing season length (GSL) in response to a doubling of CO_2 (*left*) and corresponding regional uncertainties (*right*) for regions defined in Table 2. Grid points where the response is significant at 95% confidence level in the majority of members are stippled

6.3 Frost days and growing season length

The number of frost days (FD) is relevant for impacts on vegetation, snow melting and freezing/thawing of the soil. The ensemble mean response to a doubling of CO_2 (Fig 11a) is largest at around 60°N. The response further north is smaller since the DJF temperatures do not exceed freezing point despite stronger warming. The response pattern here is consistent with transient simulations for the twenty-first century (Tebaldi et al. 2006). CLMCUBE reveals large uncertainties induced by the snow albedo parametrization in particular in Western North America and Northern Europe (Fig 11b).

Growing season length (GSL) is not an extreme index per se. It provides a rough estimate on the length of the period favorable for vegetation growth. Note that GSL is temperature dependent and does not account for any water limitation in vegetation growth. In contrast to the other indices used here, GSL is most sensitive to spring and autumn temperatures. Since GSL is only meaningful for extratropical regions, we do not show any changes between 30°N and 30°S. The entire northern mid-latitudes experience a significant increase in GSL in response to $2 \times CO_2$. Particularly over the western parts of the continents the GSL is extended by more than 1.5 months. The GSL response involves large uncertainties (more than 3 weeks) particularly due to the vegetation onset in spring, which is sensitive to the timing of the snow melt and thus to the snow albedo perturbations. Over Northern Europe the growing season under $2 \times CO_2$ starts 26–46 days earlier than in present-day conditions.

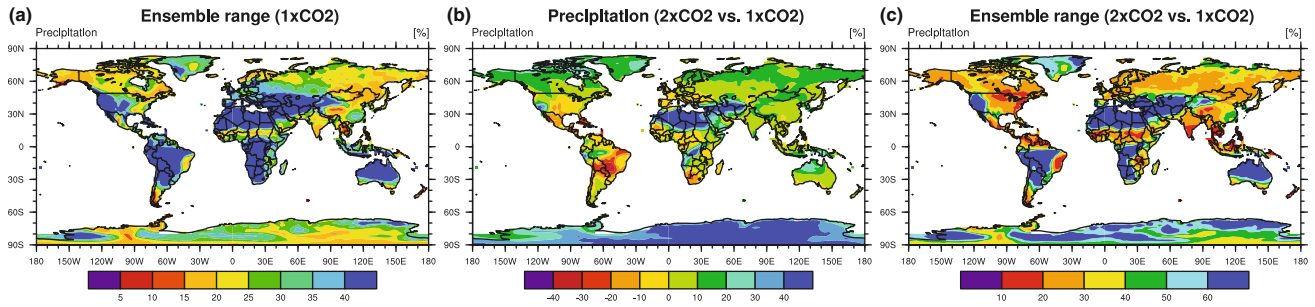

Fig. 12 **a** CLMCUBE ensemble range (95th–5th percentile member) of present-day JJA precipitation. The range is shown as a relative departure from the local climatology. **b** Ensemble mean JJA precipitation response to doubling of CO_2 and (**c**) corresponding uncertainty range relative to ensemble mean response (5th–95th percentile, *right panel*)

Table 3 Role of different land surface parameter in explaining ensemble range of summer (JJA for Northern Hemisphere and DJF for Australia) precipitation derived from multiple linear regression

The total adjusted variance [%] is given in the first column and the partial variance [%] explained by each parameter in the following columns

	Total expl. var.	Veg. albedo	Snow albedo	Water table	V_{max}	Roughn. length
Summer precip.						
AUS	62.0	52.0	0.2	0.5	5.5	5.5
AMZ	65.8	59.0	2.5	3.7	1.2	1.0
WNA	86.3	4.3	2.7	50.5	29.3	0.1
CNA	90.3	14.6	1.2	25.0	48.3	1.8
ENA	83.3	60.5	1.0	0.0	22.5	0.1
MED	84.0	12.8	0.3	48.2	19.9	3.6
NEU	89.9	12.2	0.1	27.2	50.5	0.4
WAF	53.8	42.8	0.0	11.8	1.3	0.0
SAS	74.7	59.7	4.3	6.8	2.1	3.1
CAS	45.6	0.0	9.5	31.5	4.9	2.1
NAS	92.3	16.5	8.8	11.7	55.0	0.7

7 Sensitivity of present-day precipitation and response

Regarding precipitation, we only evaluate the ensemble range for summer (Fig. 12a), which due to the important role of convective processes is most sensitive to land surface parameterizations. The relative ensemble range with respect to the ensemble mean is largest over dry regions, which to some extent is a result of the low baseline values. Present-day summer precipitation is substantially reduced in members with low V_{max} (over vegetated mid-latitudes e.g. Central North America) and in members with a deep water table (over dry subtropical regions, e.g. Mediterranean and Central Asia) (Fig. S5). Table 3 illustrates that the role of the land surface parameter in explaining the precipitation variance across CLMCUBE differs across regions with V_{max}, water table depth and vegetation albedo being most important. The uncertainty of the mean induced by internal variability accounts for approximately 5–30% of the uncertainty range (Fig. S8a).

The global mean land precipitation response (ΔP_{ANN}) to a doubling of CO_2 ranges from +5.4–8.4%. While present-day precipitation and temperature are highly correlated, we do not find a significant correlation between ΔP_{ANN} and ΔT_{ANN} across CLMCUBE. The spatial pattern mean response (Fig. 12b) compares well with the CMIP3 ensemble transient response. The CLMCUBE ensemble mean is consistent in sign, wherever CMIP3 shows a highly robust precipitation change (more than 90% agreement in sign across models), except for some particularly dry regions. For parts of north Africa and over south-central Africa at about 10–20°S CLMCUBE simulates a tendency to wetter conditions, which contrasts with the majority of the CMIP3 models.

Note that the relative ΔP involves large uncertainties particularly during JJA (Fig 12c). The range in the relative precipitation response ΔP_{JJA} is largest over the subtropical regions of both hemispheres. Over very dry regions the large relative range should not be overinterpreted as it is to some extent a result of the small baseline present-day values. However, even in many mid-latitudinal regions parameter perturbations can change the sign of ΔP_{JJA}. ΔP_{JJA} ranges between −14 and +5% in Central North America, −9 and +20% in the Mediterranean region, or −6 and +36% in Central Asia.

Note that given the short length of the simulation internal variability can induce large uncertainties in the

mean response. We tested this by randomly sampling the corresponding number of years for 1 × CO_2 and 2 × CO_2 with a Monte Carlo technique from a 50-year control experiment performed with the unperturbed model. We find that the majority of the uncertainty in ΔP at the grid scale is induced by internal variability as demonstrated in Fig. S8b. Internal variability dominates especially over the tropics whereas over mid- to high-latitudes parameter uncertainties play an important role. In general, the sensitivity of ΔP_{JJA} to the different parameters is highly nonlinear.

8 Conclusions

We present a systematic analysis of uncertainties in the climate response to a doubling of atmospheric CO_2 concentrations based on CLMCUBE, a perturbed land surface parameter experiment. CLMCUBE includes 108 versions of CCSM 3.5 (mixed-layer ocean), in which five poorly constrained land surface parameters are perturbed across their nominal ranges, individually and in all possible combinations of the the discrete parameter values sampled.

We find that land surface parameter induce small uncertainties at global scale, substantial uncertainties at regional and seasonal scale and very large uncertainties in the tails of the distribution, the climate extremes. Land surface parameters are revealed to control the response not only of the mean but also of the variability of temperature.

- *Global response:* The global land temperature response to a doubling of atmospheric CO_2 concentrations ranges between 2.47–2.87 K across CLMCUBE. Thereby the range is substantially smaller than in equivalent ensembles with perturbed atmospheric parameters. The differences here are mainly a result of perturbations of an empirical snow aging parameter, which controls the snow albedo feedback. We find that members with high present-day snow albedo show a stronger decrease in albedo and snow cover fraction and thus a stronger warming. This confirms an earlier hypothesis based on a small set of GCMs (Levis et al. 2007).
- *Cold extremes:* The climate change signal of temperature extremes varies strongly across CLMCUBE as a result of land surface parameter and initial condition uncertainties. The response in DJF 5th percentile, here referred to as cold extremes, ranges between 1.9–8.8 K in Northern Europe and 3.0–8.3 K in North Asia. Thereby the CLMCUBE range exceeds the spread across the CMIP3 multi-model ensemble over the two regions. The large uncertainty range results from the fact that the response in temperature mean and daily variability tend to line up in winter. Both variability and the mean response relate to the amount of snow cover/surface albedo reduction. Members with strong (weak) snow albedo feedback simulate strong (weak) warming and strongly (weakly) reduced variability. As a result mean and variability combine in some members to a weak and in others to a very strong response of cold extremes over northern mid- to high-latitudes. Changes in cold extremes and frost days are highly uncertain in these regions, where they have important socio-economic and ecological impacts, e.g. on energy demand (Hadley et al. 2006) or mortality of mountain pine beetle (Stahl et al. 2006). Furthermore, the shift in timing of spring snow melt, which affects the vegetation onset is highly sensitive to the choice of the snow aging parameter. As are result the climate change signal in growing season length is highly uncertain and differs by a factor of almost 2 across CLMCUBE (i.e. 25–45 days increase).
- *Hot extremes:* The uncertainty in hot extremes (95th percentile of summer temperatures) exceeds the uncertainty in the mean summer warming by far. However, the range here is smaller than the CMIP3 uncertainty range for hot extremes. Again, variability plays an important role, for instance, in the Mediterranean region and central North America, where it increases in response to 2 × CO_2. More intense and frequent hot extremes may have substantial effects on human health. Three specific health indicators have been analysed here. Heat wave duration and heat index response involve substantial uncertainties (response varies by a factor 2–3), whereas the response in tropical nights is relatively insensitive to land surface parameter perturbations.
- *Precipitation:* For the precipitation response, the CLMCUBE range is often larger than the mean signal, especially in dry regions. Given the short simulation length, a large portion of this precipitation uncertainty is induced by natural variability. Over the Mediterranean, Central North America and Australia even the sign of the summer precipitation response to a doubling of CO_2 varies between ensemble members. This result is interesting since it is not consistent with the transient response of CCSM3.0 nor the majority of the CMIP3 models for the twenty-first century, in which robust precipitation reductions are identified over the Mediterranean and parts of Australia. The uncertainty range found here should not be overinterpreted since potentially important changes in ocean circulation and SST variability are not reflected in the mixed-layer ocean model and the simulations are relatively short given the natural variability of summer precipitation.

Note that this experiment only covers part of the actual uncertainty range (i.e. uncertainties induced by land

surface model parameters). First, because feedback uncertainties in other components of the climate system, such as atmosphere feedbacks (water vapour, cloud and lapse rate), have not been accounted for. Joint perturbations in atmospheric and land surface parameters may further lead to non-linear effects, which are not sampled here. Second, only a subset of the land surface parameter uncertainty has been perturbed, excluding uncertainties in the biogeochemical feedbacks, which are not interactively simulated in this model version. Uncertainties in the carbon/nitrogen cycle may be relevant for climate-carbon cycle feedbacks and uncertainties in the carbon uptake by the land biosphere. Third, potentially important structural uncertainties in grid resolution and fundamental physical assumptions in the model formulation have not been considered.

CLMCUBE provides extended insight in the global and regional uncertainties related to land surface parameterizations. While uncertainties are large particularly in the case of temperature extremes, the sign of the response is very robust for temperature-related variables.

Acknowledgments We thank Gerald Meehl, Keith Oleson and Reto Knutti for the fruitful discussion and the anonymous reviewers for their valuable comments on the manuscript. Erich Fischer was supported by the Swiss National Science Foundation. Support of this dataset is provided by the Office of Science, U.S. Department of Energy.

References

Alexander L, Zhang X, Peterson T, Caesar J, Gleason B, Tank AK, Haylock M, Collins D, Trewin B, Rahimzadeh F, Tagipour A, Kumar K, Revadekar J, Griffiths G, Vincent L, Stephenson D, Burn J, Aguilar E, Brunet M, Taylor M, New M, Zhai P, Rusticucci M, Vazquez-Aguirre J (2006) Global observed changes in daily climate extremes of temperature and precipitation. J Geophys Res 111. doi:10.1029/2005JD006290

Allen M, Stott P, Mitchell J, Schnur R, Delworth T (2000) Quantifying the uncertainty in forecasts of anthropogenic climate change. Nature 407:617–620

Barnett DN, Brown SJ, Murphy JM, Sexton DMH, Webb MJ (2006) Quantifying uncertainty in changes in extreme event frequency in response to doubled CO2 using a large ensemble of GCM simulations. Clim Dyn 26. doi:10.1007/s00382-005-0097-1

Beniston M (2004) The 2003 heat wave in Europe: a shape of things to come? An analysis based on Swiss climatological data and model simulations. Geophys Res Lett 31. doi:10.1029/2003GL018857

Breiman L, Friedman J, Olshen R, Stone C (1984) Classification and regression trees. Wadsworth, Belmont, CA 1

Burke E and Brown S (2008) Evaluating uncertainties in the projection of future drought. J Hydrometeorol 9:292–299

Caesar J, Alexander L, Vose R (2006) Large-scale changes in observed daily maximum and minimum temperatures: creation and analysis of a new gridded data set. J Geophys Res 111. doi:10.1029/2005JD006280

Clark RT, Brown SJ, Murphy JM (2006) Modeling Northern Hemisphere summer heat extreme changes and their uncertainties using a physics ensemble of climate sensitivity experiments. J Clim 19:4418–4435

Dai A, Trenberth K, and Karl T (1999) Effects of clouds, soil moisture, precipitation, and water vapor on diurnal temperature range. J Clim 12:2451–2473

Easterling D, Evans J, Groisman P, Karl T, Kunkel K, Ambenje P (2000) Observed variability and trends in extreme climate events: a brief review. Bull Am Meteorol Soc 81:417–425

ECMWF (2007) IFS documentation—Cy31r1: part IV, physical processes. ECMWF, Full scientific and technical documentation. http://www.ecmwf.int/research/ifsdocs/CY31r1/index.html

Fischer EM, Schär C (2009) Future changes in daily summer temperature variability: driving processes and role for temperature extremes. Clim Dyn. doi:10.1007/s00382-008-0473-8

Fischer EM, Schär C (2010) Consistent geographical patterns of changes in high-impact european heatwaves. Nat Geosci. doi:10.1038/NGEO866

Frich P, Alexander L, Della-Marta P, Gleason B, Haylock M, Tank A, Peterson T (2002) Observed coherent changes in climatic extremes during the second half of the twentieth century. Clim Res 19:193–212

Gent P, Yeager S, Neale R, Levis S, Bailey D (2010) Improvements in a half degree atmosphere/land version of the CCSM. Clim Dyn 34(6):819–833

Gregory J and Mitchell J (1995) Simulation of daily variability of surface temperature and precipitation over Europe in the current and 2 × CO_2 climates using the UKMO climate model. Q J R Meteorol Soc 121:1451–1476

Grize L, Huss A, Thommen O, Schindler C, Braun-Fahrländer C (2005) Heat wave 2003 and mortality in Switzerland. Swiss Med Wkly 135:200–205

Hadley S, Hernandez J, Broniak C, Blasing T (2006) Responses of energy use to climate change: a climate modeling study. Geophys Res Lett 33:L17703

Hawkins E and Sutton R (2009) The potential to narrow uncertainty in regional climate predictions. Bull Am Meteorol Soc 90:1095–1107

Hémon D, Jougla E, Laurent CJF, Bellec S, Pavillon G (2003) Surmortalité liéeàla canicule d'août 2003 en France. Bull Epidémiologique Hebdomadaire 45–46:1–5

IPCC (2007) Climate change 2007: the physical science basis. Contribution of working group i to the fourth assessment report of the intergovernmental panel on climate change. Cambridge University Press, Cambridge, 996 pp

Katz RW and Brown BG (1992) Extreme events in a changing climate: variability is more important than averages. Clim Change 21:289–302

Kharin V, Zwiers F, Zhang X, Hegerl G (2007) Changes in temperature and precipitation extremes in the IPCC ensemble of global coupled model simulations. J Clim 20:1419–1444

Knutti R, Allen M, Friedlingstein P, Gregory J, Hegerl G, Meehl G, Meinshausen M, Murphy J, Plattner G, Raper S et al (2008) A review of uncertainties in global temperature projections over the twenty-first century. J Clim 21:2651–2663

Koster R, Dirmeyer P, Hahmann A, Ijpelaar R, Tyahla L, Cox P, Suarez M (2002) Comparing the degree of land-atmosphere interaction in four atmospheric general circulation models. J Hydrometeor 3:363–375

Kunkel K, Andsager K, Easterling D (1999) Long-term trends in extreme precipitation events over the conterminous United States and Canada. J Clim 12:2515–2527

Lawrence D, Thornton P, Oleson K, Bonan G (2007) The partitioning of evapotranspiration into transpiration, soil evaporation, and canopy evaporation in a GCM: impacts on land-atmosphere interaction. J Hydrometeor 8:862–880

Levis S, Bonan G, Lawrence P (2007) Present-day springtime high-latitude surface albedo as a predictor of simulated climate sensitivity. Geophys Res Lett 34:L17703

Liu Y, Gupta H, Sorooshian S, Bastidas L, Shuttleworth W (2005) Constraining land surface and atmospheric parameters of a locally coupled model using observational data. J Hydrometeor 6:156–172

Meehl G, Covey C, Taylor K, Delworth T, Stouffer R, Latif M, McAvaney B, Mitchell J (2007) The WCRP CMIP3 multimodel dataset:A new era in climate change research. Bull Am Meteorol Soc 88:1383–1394

Meehl G, Zwiers F, Evans J, Knutson T, Mearns L, Whetton P (2000) Trends in extreme weather and climate events: issues related to modeling extremes in projections of future climate change. Bull Am Meteorol Soc 81:427–436

Meehl GA and Tebaldi C (2004) More intense, more frequent, and longer lasting heat waves in the 21st century. Science 305:994–997

Murphy J, Sexton D, Barnett D, Jones G, Webb M, Collins M, Stainforth D (2004) Quantification of modelling uncertainties in a large ensemble of climate change simulations. Nature 430:768–772

Niu G, Yang Z, Dickinson R, Gulden L (2005) A simple TOPMOD-EL-based runoff parameterization (SIMTOP) for use in global climate models. J Geophys Res 110. doi:10.1029/2005JD006111

Niu G, Yang Z, Dickinson R, Gulden L, Su H (2007) Development of a simple groundwater model for use in climate models and evaluation with Gravity Recovery and Climate Experiment data. J Geophys Res 112. doi:10.1029/2006JD007522

Oleson K, Dai Y, Bonan G, Bosilovich M, Dickinson R, Dirmeyer P, Hoffman F, Houser P, Levis S, Niu G et al (2004) Technical description of the community land model (CLM). Tech Note NCAR/TN-461+ STR

Oleson K, Niu G, Yang Z, Lawrence D, Thornton P, Lawrence P, Stockli R, Dickinson R, Bonan G, Levis S et al (2008) Improvements to the Community Land Model and their impact on the hydrological cycle. J Geophys Res 113. doi:10.1029/2007JG000563

Piani C, Frame D, Stainforth D, Allen M (2005) Constraints on climate change from a multi-thousand member ensemble of simulations. Geophys Res Lett 32:23

Qu X and Hall A (2006) Assessing snow albedo feedback in simulated climate change. J Clim 19:2617–2630

Qu X and Hall A (2007) What controls the strength of snow-albedo feedback? J Clim 34:3971–3981

Räisänen J (2002) CO2-induced changes in interannual temperature and precipitation variability in 19 CMIP2 experiments. J Clim 15:2395–2411

Räisänen J and Joelsson R (2001) Changes in average and extreme precipitation in two regional climate model experiments. Tellus A 53:547–566

Sanderson BM (2010) A multi-model study of parametric uncertainty in predictions of climate response to rising greenhouse gas concentrations. J Clim. doi:10.1175/2010JCLI3498.1

Schär C, Vidale PL, Lüthi D, Frei C, Häberli C, Liniger MA, Appenzeller C (2004) The role of increasing temperature variability in European summer heatwaves. Nature 427:332–336. doi:10.1038/nature02300

Seneviratne SI, Koster RD, Guo Z, Dirmeyer PA, Kowalczyk E, Lawrence D, Liu P, Lu C-H, Mocko D, Oleson KW, Verseghy D (2006a) Soil moisture memory in AGCM simulations: analysis of global land-atmosphere coupling experiment (GLACE) data. J Hydrometeor 7:1090–1112

Seneviratne SI, Lüthi D, Litschi M, Schär C (2006b) Land-atmosphere coupling and climate change in Europe. Nature 443:205–209

Stahl K, Moore R, McKendry I (2006) Climatology of winter cold spells in relation to mountain pine beetle mortality in British Columbia, Canada. Clim Res 32:13–23

Stainforth D, Aina T, Christensen C, Collins M, Faull N, Frame D, Kettleborough J, Knight S, Martin A, Murphy J et al (2005) Uncertainty in predictions of the climate response to rising levels of greenhouse gases. Nature 433:403–406

Steadman RG (1984) A universal scale of apparent temperature. J Clim Appl Meteorol 23:1674–1687

Stöckli R, Lawrence D, Niu G, Oleson K, Thornton P, Yang Z, Bonan G, Denning A, Running S (2008) Use of FLUXNET in the Community Land Model development. J Geophys Res 113. doi:10.1029/2007JG000562

Tebaldi C, Hayhoe K, Arblaster J, and Meehl G (2006) Going to the extremes. Clim Change 79:185–211

Tebaldi C and Knutti R (2007) The use of the multi-model ensemble in probabilistic climate projections. Philos Transact A Math Phys Eng Sci 365:2053

Thornton P and Zimmermann N (2007) An improved canopy integration scheme for a land surface model with prognostic canopy structure. J Clim 20:3902–3923

Vidale PL, Lüthi D, Wegmann R, Schär C (2007) Europea summer climate variability in a heterogeneous multi-model ensemble. Clim Change 81:209–232

Weisheimer A and Palmer T (2005) Changing frequency of occurrence of extreme seasonal temperatures under global warming. Geophys Res Lett 32:L20721

White M, Thornton P, Running S, Ramakrishna R (2000) Parameterization and sensitivity analysis of the BIOME-BGC terrestrial ecosystem model: net primary production controls. Earth Interact 4:1